buildings

MDPI

Article

Multi-Variable Optimization of Sustainable Alkali-Activated Mortar with High Waste Concrete Powder Dosage for Enhanced Drying Shrinkage Resistance

Zhen Zou [1], Han Gao [2,*], Yingda Zhang [3], Jiehong Li [4], Miao Li [5] and Yang Yu [1,2,6,*]

[1] School of Materials Science and Engineering, Shenyang University of Technology, Shenyang 110870, China; zouzhen@smail.sut.edu.cn
[2] Centre for Infrastructure Engineering and Safety, The University of New South Wales, Sydney, NSW 2052, Australia
[3] School of Architecture and Civil Engineering, Xihua University, Chengdu 610039, China; yingda.Zhang@xhu.edu.cn
[4] School of Civil and Hydraulic Engineering, Chongqing University of Science and Technology, Chongqing 401331, China; jiehong.li@unswalumni.com
[5] School of Computing, Mathematics and Engineering, Faculty of Business, Justice and Behavioral Sciences, Charles Sturt University, Bathurst, NSW 2795, Australia; mli@csu.edu.au
[6] Centre for Infrastructure Engineering, Western Sydney University, Penrith, NSW 2751, Australia
* Correspondence: han.gao1@unsw.edu.au (H.G.); y.yu3@westernsydney.edu.au (Y.Y.)

Abstract

This study presents a comprehensive strategy for mitigating drying shrinkage of alkali-activated slag mortar (AASM) with the high-dosage incorporation of waste concrete powder (WCP). Response surface methodology (RSM) coupled with microstructural analysis is used to investigate the synergistic effects of WCP particle size (R), activator modulus (AM), activator content (AC), and water to solid ratio (W/S) on shrinkage behavior and matrix development. The optimized mix—WCP-R = 33.6 μm, AM = 1.23, AC = 6.03%. and W/S = 0.49—exhibits a 120-day drying shrinkage of only 1450.1 με, significantly lower than that of conventional AASM. Microstructural observations reveal that coarser WCP particles act predominantly as fillers, enhancing stability, whereas finer particles promote gel formation but increase shrinkage. A high AM (1.6) refines the pore structure by reducing large pores (>0.05 μm), while a low W/S (0.46) decreases total porosity to 7.67%, collectively restricting moisture transport. The coexistence of C-(A)-S-H gel and hydrotalcite improves matrix integrity. Notably, this optimized HWAASM achieves a substantially reduced carbon footprint of 180 kg CO_2-eq/t, underscoring its significant environmental advantage. The findings advance the understanding of shrinkage mechanisms in high-WCP-AASM and offer an eco-friendly route for valorizing construction waste and developing low-carbon building materials.

Keywords: high dosage waste concrete powders; alkali-activated slag; drying shrinkage; response surface method; microstructural analysis

Academic Editor: Vipul Patel

Received: 15 September 2025
Revised: 13 October 2025
Accepted: 27 October 2025
Published: 28 October 2025

Citation: Zou, Z.; Gao, H.; Zhang, Y.; Li, J.; Li, M.; Yu, Y. Multi-Variable Optimization of Sustainable Alkali-Activated Mortar with High Waste Concrete Powder Dosage for Enhanced Drying Shrinkage Resistance. *Buildings* **2025**, *15*, 3903. https://doi.org/10.3390/buildings15213903

1. Introduction

Alkali-activated materials (AAMs) are produced by activating aluminosilicate precursors using alkaline solutions, presenting an eco-friendly substitute for Portland cement owing to their reduced carbon footprint and equivalent or enhanced mechanical performance [1–4]. AAMs demonstrate superior chemical corrosion resistance [5–7] and

high-temperature performance [8], but face durability challenges including high drying shrinkage, carbonation vulnerability [9,10], and alkali–aggregate reactivity [11–13]. Waste concrete powder, a construction waste-derived material with pozzolanic potential [14,15], shows promise in mitigating these issues while reducing slag consumption (≥50% replacement) and landfill waste. However, the shrinkage behavior of high-WCP AAM systems remains poorly understood.

Compared to OPC concrete, AAS concrete shows higher drying shrinkage rates [16]. Prior studies indicate that the shrinkage characteristics of AAS concrete are influenced by the precursor materials, environmental conditions, and aggregate properties [17,18]. For instance, Aydın, S and Baradan, B [19] pointed out that the drying shrinkage rate of AAS mortar can be significantly affected by the SiO_2/Na_2O ratio (AM) and Na_2O content in the activator solution. AAS mortars activated with Na_2SiO_3 exhibited higher drying shrinkage than those activated with NaOH. Liu, C [20] found that the shrinkage rate of AAS mortars was influenced by curing conditions, with environmental and sealed conditions leading to higher shrinkage rates, with sealed conditions in particular causing significant autogenous shrinkage. Nanayakkara, O [21] discovered that both AAS-NA (natural aggregate) and AAS-RA (recycled aggregate) concrete had drying shrinkage rates exceeding the allowable limits set by standards like AS 3600:2018 [22], with AAS concrete showing a 32% increase in shrinkage after one year, which continued to increase over time. Despite its advantages in mechanical performance and sustainability, the persistent issue of high shrinkage impedes the broader adoption of AAS. While slag offers environmental advantages compared to traditional Portland cement, its production relies on by-products from the steel industry, with limited resources and some environmental burdens during extraction [23]. Moreover, the stability of slag supply could be impacted by fluctuations in steel production. In contrast, WCP was derived from the recycling and processing of waste concrete, representing a significant pathway for utilizing construction waste [24,25]. Incorporating WCP substantially decreases construction waste volumes, thus reducing environmental pollution [26]. Consequently, researchers began exploring the use of WCP as a precursor material in AAS, with the potential for WCP's particle characteristics [27] and chemical composition [28] to positively affect AAS's mechanical properties, such as enhancing compressive strength [29] and flexural strength [4], while also mitigating shrinkage issues. For instance, Sasui, S [30] found that when WCP was subjected to heat treatment and mixed with 0–50 wt% granulated blast furnace slag (GBFS), and then added to AAS concrete after being heated to 800 °C, the shrinkage of the AAS concrete was reduced. Liu, M [31] found that increasing the heat treatment temperature of WCP reduced the drying shrinkage rate of mortar, with the inclusion of WCP heat-treated at 800 °C significantly lowering shrinkage by 14.13% within 36 days. Liang, G [32] reported that the incorporation of ultrafine waste concrete powder (UWCP) into alkali-activated binders (AABs) effectively reduced both autogenous and drying shrinkage, with 9 wt% UWCP lowering the drying shrinkage rate by 27.87% after 56 days. Zhang, D [4] systematically examined the drying shrinkage of AAS foam concrete by incorporating partial WCP replacement. They found that an initial increase in WCP content reduced drying shrinkage, with the lowest shrinkage at a 30% replacement level, but exceeding this level resulted in increased shrinkage. It was observed that most research focused on WCP replacement rates of between 10% and 30% and explained the mechanisms by which low-content WCP influenced AAS shrinkage. It can be observed that existing studies mostly focus on the improvement of AAS performance with low-content WCP. Although low-level WCP (≤30%) has been examined as an AAS performance enhancer, the quantitative links and underlying mechanisms through which the particle size effects of high-level WCP (≥50%) interact with key activator parameters to influence long-term drying shrinkage remain little

understood. Given the complexity of this multi-variable system, traditional trial-and-error approaches are inefficient; therefore, this study employs response surface methodology to elucidate and optimize these interactions, addressing the high-shrinkage challenge of high-WCP AASM.

RSM is a statistical technique used for optimizing complex systems [33,34]. It has been effectively applied to concrete mix design [35,36], and its use in AAS optimization could help to identify the best mix design for long-term durability. Therefore, building on preliminary experiments, in an innovative approach, this study employs 60% WCP combined with 40% ground granulated blast furnace slag as precursors, along with sodium hydroxide and sodium silicate as activators, to produce HWAASM. Based on the results of the Box–Behnken Design (BBD) from RSM, the interactive effects of WCP-R, AM, AC, and W/S on the drying shrinkage behavior of HWAASM are analyzed. Additionally, XRD, TGA, MIP, and SEM tests were used to investigate the reaction products, pore distribution, and matrix uniformity of HWAASM, evaluating how these mix design elements influence the transformation of reaction products, pore structure distribution, and matrix uniformity. This study aims to systematically explore the interactive effects of these design parameters on the drying shrinkage performance of HWAASM, providing insights for developing more durable and sustainable building materials.

2. Raw Materials and Methods

2.1. Material

The GGBFS is obtained from Shengbowei New Material Co., Ltd., in Zhengzhou, China. The WCP is derived from 10-year-old, demolished road concrete. The waste concrete was manually processed: the waste concrete was first broken down into coarse fragments with a crusher, followed by pulverization into fine powder via a planetary ball mill. Finally, the WCP is obtained by sieving the ground particles through a 0.15 mm standard sieve. As shown in Figure 1, WCP exhibits irregular blocky structures with adhered fragments of old cement paste, while GGBFS displays relatively flat, flaky structures.

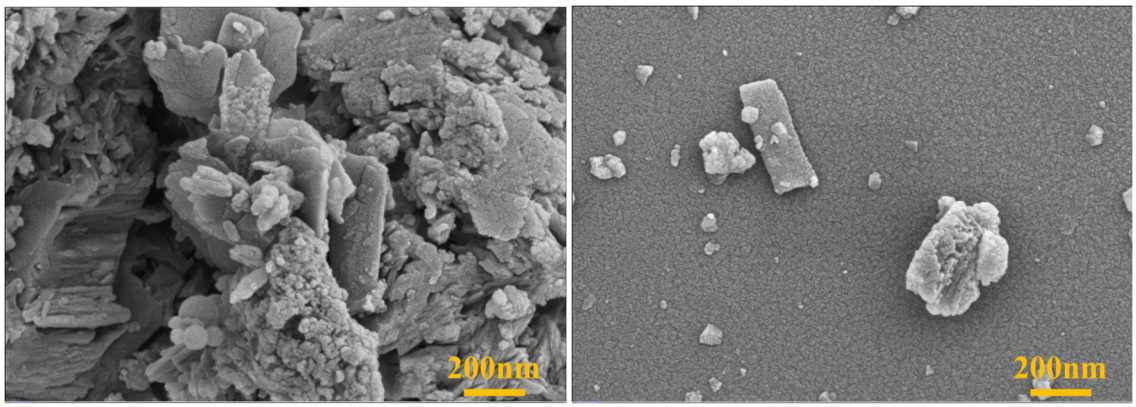

(**a**) (**b**)

Figure 1. Micromorphology of the precursor materials: (**a**) WCP; (**b**) GGBFS.

The chemical profiles of WCP and GGBFS are summarized in Table 1, with their particle size distributions provided in Table 2 and Figure 2. The mineral compositions of WCP and GGBFS, displayed in Figure 3, show that GGBFS contains small amounts of crystalline phases such as quartz and calcite, along with a broad hump observed at low angles. In contrast, WCP exhibits more crystalline phases, including quartz, calcite, and portlandite, with sharper diffraction peaks indicating a higher degree of crystallinity. The amorphous content of WCP is 23.9%, while that of GGBFS is 88.7%, indicating that GGBFS has higher

potential reactivity. Fine aggregate consists of river sand, which has a fineness modulus of 2.68 and particle sizes between 0.5 and 1 mm. The water absorption capacity is below 2%. The aggregate to binder ratio is 3. Sodium silicate (Na_2SiO_3) powder and sodium hydroxide (NaOH) granules are employed as alkaline activators. The Na_2SiO_3 (purity > 98.5%) is procured from Gongyi Borun Refractory Materials Co., Ltd., in Zhengzhou, China, containing 54.1% SiO_2 and 24.2% Na_2O (SiO_2/Na_2O = 2.3). The NaOH, of analytical grade, is provided by Shenyang Hualian Reagent Factory, with a NaOH content of no less than 96%.

Table 1. Composition and percentage content of the precursors (%).

	SiO_2	Al_2O_3	CaO	Fe_2O_3	SO_3	MgO	K_2O	Na_2O	TiO_2	MnO	Other
WCP	39.50	8.97	35.99	5.46	1.31	5.30	1.86	0.38	0.45	0.09	0.34
GGBFS	31.5	16.73	40.72	0.3	0.25	6.44	0.38	0.07	1.35	0.47	1.79

Table 2. Experimental factors and levels of variables.

Variable Factors	Levels		
	1	2	3
WCP-R	15.2 μm	24.4 μm	33.6 μm
AM	1.2	1.4	1.8
AC	6%	7%	8%
W/S	0.46	0.48	0.5

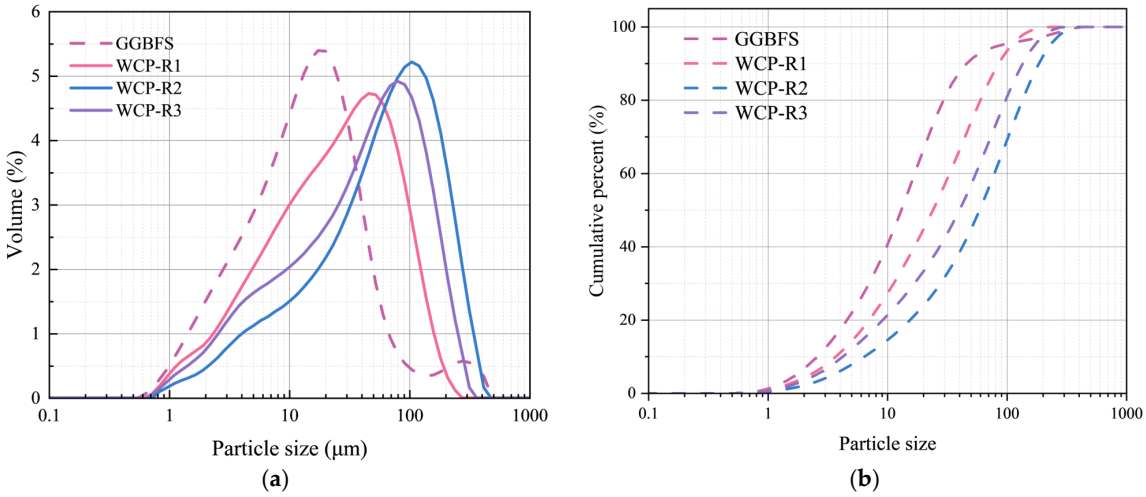

Figure 2. The particle size distribution of GGBFS and WCP: (**a**) differential; (**b**) cumulative percent passing.

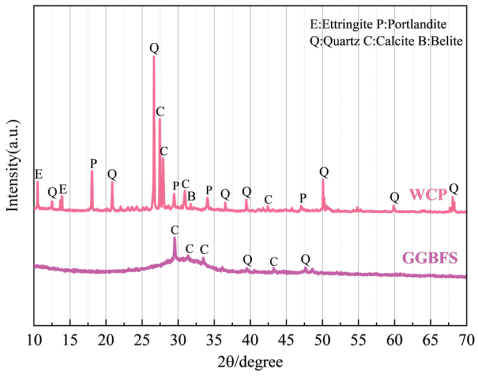

Figure 3. The phase composition of WCP and GGBFS: Ettringite [$3CaO{\cdot}Al_2O_3{\cdot}3CaSO_4{\cdot}32H_2O$]; Portlandite [$Ca(OH)_2$]; Quartz [$SiO_2$]; Calcite [$CaCO_3$]; Belite [$C_2S$].

2.2. Mix Design and Preparation

Huo, W et al. [37] report that mixes containing 50% recycled concrete fine powder (RCFP) reach a 28-day compressive strength of 59.05 MPa, while Liu, M et al. [38] observe that when the WCP replacement rate reaches 50%, the drying shrinkage of mortar remains comparable to that of conventional slag-based geopolymer mortar. However, high-dosage WCP (>50%) significantly increases shrinkage due to amplified amorphous phase formation and pore connectivity [39,40]. Preliminary results show a clear inflection point in drying shrinkage behavior at 60% replacement, where the increase in shrinkage accelerates sharply compared with lower dosages, marking 60% as a critical threshold. Consequently, this study fixes the WCP replacement level at 60%. The levels of experimental variables are selected based on the following rationale: WCP-R = 15.2–33.6 μm covers typical ranges in existing studies [27,28], balancing the reactivity of fine particles while leveraging the filler effect of coarse particles; AM = 1.2–1.6 references Aydin, S et al. [19], using 1.4 as the central point to verify its shrinkage-minimizing effect; AC = 6–8% builds on Fang, S et al. [17] to avoid shrinkage surge from excessive alkali content; and W/S = 0.46–0.50 is determined through preliminary experiments. This research applies RSM to optimize the interplay of four critical parameters affecting drying shrinkage in alkali-activated slag mortar: WCP-R, AM, AC, and W/S—details in Table 2.

A Box–Behnken Design with four factors and three levels was implemented using Design Expert 11 software, generating 29 experimental runs to capture quadratic relationships among variables while minimizing experimental workload [41,42]. The 120-day shrinkage value in Table 3 has been designated as the dependent variable for analysis.

Table 3. The result of BBD experiments.

Serial Number	Sample Number	WCP-R (μm)	AM	AC (%)	W/S	Shrinkage Strain (με)
1	R2M2A2W2	24.4	1.4	7	0.48	13,842.3
2	R1M2A1W2	15.2	1.4	6	0.48	11,734.7
3	R3M3A2W2	33.6	1.6	7	0.48	14,239.3
4	R3M2A3W2	33.6	1.4	8	0.48	10,785.1
5	R1M2A2W1	15.2	1.4	7	0.46	10,489.4
6	R1M1A2W2	15.2	1.2	7	0.48	12,669.3
7	R2M2A1W3	24.4	1.4	6	0.5	10,251.4
8	R2M3A2W1	24.4	1.6	7	0.46	18,423.2
9	R3M2A1W2	33.6	1.4	6	0.48	8556.2
10	R1M2A2W3	15.2	1.4	7	0.5	15,918.9
11	R1M2A3W2	15.2	1.4	8	0.48	11,993.7
12	R2M2A2W1	24.4	1.4	8	0.46	11,594.1
13	R2M2A2W2	24.4	1.4	7	0.48	11,696.3
14	R2M2A3W3	24.4	1.4	8	0.5	2220.4
15	R2M2A2W2	24.4	1.4	7	0.48	11,864.2
16	R2M1A3W2	24.4	1.2	8	0.48	6613.6
17	R3M1A2W2	33.6	1.2	7	0.48	11,349.1
18	R2M2A2W2	24.4	1.4	7	0.48	12,845.5
19	R2M1A2W1	24.4	1.2	7	0.46	3671.8
20	R3M2A2W1	33.6	1.4	7	0.46	13,948.1
21	R2M2A2W2	24.4	1.4	7	0.48	10,824.4
22	R1M3A2W2	15.2	1.6	7	0.48	14,239.2
23	R2M3A2W3	24.4	1.6	7	0.5	1682.2
24	R2M3A3W2	24.4	1.6	8	0.48	10,838.9
25	R3M2A2W3	33.6	1.4	7	0.5	6788.4
26	R2M1A2W3	24.4	1.2	7	0.5	11,458.2
27	R2M3A1W2	24.4	1.6	6	0.48	7432.7
28	R2M2A1W1	24.4	1.4	6	0.46	3098
29	R2M1A1W2	24.4	1.2	6	0.48	6615.1

In the 24 h before the experiment, the solid powdered Na_2SiO_3 is dissolved in 21.7% water to prepare a Na_2SiO_3 solution. Then, the required amount of solid granular NaOH is added to the Na_2SiO_3 solution to prepare the alkali activator solution, which is cooled for 24 h. According to JGJ/T 98 (2011) [43], the mix proportions of the alkali-activated mortar are designed, as shown in Table 4. Precise quantities of the raw materials and river sand, as per the predetermined mix designs, are measured out and then stored in a drying chamber at 65 °C for a duration of 24 h. This process aims to eliminate both the physically bound moisture and any excess water present within the materials. The dried WCP and GGBFS are then mixed in a JJ-20H mixer (Cangzhou Xinke Construction Instrument Co., Ltd., Xian County Industrial Park, Cangzhou City, Hebei Province, China) for 20 s; dried river sand is added, and the mixture is stirred for 60 s. Next, the required amount of pure water (subtracting the water content in the activator solution) is added, and the mixture is stirred for 120 s. In compliance with JGJ/T 70 (2009) [44], shrinkage tests use prismatic specimens of dimensions 40 mm × 40 mm × 160 mm, each featuring two 6.5 mm holes centered on their end faces. The shrinkage heads are fixed in the holes on both ends of the mold, with 8 ± 1 mm of the shrinkage head exposed from the specimen's surface. The freshly mixed mortar is placed into the mold and compacted using a cement mortar vibrating table. The mortar is cured with the mold for 7 days under conditions of 20 ± 2 °C temperature and over 90% relative humidity. After 7 days, the molds are removed, and the specimens are labeled with the test direction. Using the same mix proportions but without river sand, 40 mm cubic specimens were produced with an NJ-160 cementitious paste mixer (Shanghai Wanlian Equipment Technology Co., Ltd., Jiading Business District, Shanghai, China). The specimens are cured for 28 days under the same curing conditions mentioned above for microstructural characterization tests.

Table 4. Results of variance analysis of 120-day drying shrinkage model of HWAASM.

Source	Sum of Squares	Mean Square	F-Value	*p*-Value
Model	4.496×10^8	3.211×10^7	25.95	<0.0001
A	1.079×10^7	1.079×10^7	8.72	0.0105
B	1.747×10^7	0.1747	14.11	0.0021
C	3.368×10^6	3.368×10^6	7.72	0.1212
D	1.388×10^7	1.388×10^7	11.21	0.0048
AB	4.358×10^5	4.358×10^5	0.3522	0.5624
AC	9.700×10^5	9.700×10^5	0.7838	0.3909
AD	3.962×10^7	3.962×10^7	32.02	<0.0001
BC	2.903×10^6	2.903×10^6	2.35	0.1479
BD	1.504×10^8	1.504×10^8	121.53	<0.0001
CD	6.829×10^7	6.829×10^7	55.18	<0.0001
A2	2.275×10^7	2.275×10^7	18.38	0.0008
B2	7.315×10^6	7.315×10^6	5.91	0.0291
C2	6.848×10^7	6.848×10^7	55.34	<0.0001
D2	3.351×10^7	3.351×10^7	27.08	0.0001
Lack of Fit	1.195×10^7	1.195×10^6	0.8902	0.6012

2.3. Test Methods

2.3.1. Drying Shrinkage Test

The drying shrinkage of the specimens is measured according to the shrinkage test method specified in the Chinese standard JGJ/T 70-2009 [44]. Upon completion of the curing phase, the test samples are transferred to a controlled setting, before initial length measurement with an SP-176 vertical shrinkage tester (Cangzhou Huaxing Jiancai Testing Instrument Co., Ltd., Cangzhou, Hebei Province, China); specimens are acclimated for 4 h

at 20 ± 2 °C and 60 ± 5% relative humidity. The changes in length of the mortar samples are recorded, starting from the second day to 120 days. Equation (1) describes the shrinkage strain at the corresponding age of the sample.

$$\varepsilon_i = \frac{L_0 - L_i}{L_0} \quad (1)$$

where ε_i denotes the natural drying shrinkage (με), L_0 is the initial specimen length measured 2 days after molding (mm), and L_i refers to the length at the test age.

2.3.2. Microscopic Characterization Tests

First, all microstructural testing samples are immersed in isopropanol (analytical grade) for one week to block the continued hydration of unreacted alkaline substances. Afterward, the samples are removed and dried in a 50 °C constant-temperature oven for 24 h to remove residual solvents and free water. Finally, depending on the testing requirements, the dried samples are either ground into powder for XRD, TGA, and MIP or cut into small pieces for SEM.

Phase identification is carried out by X-ray diffraction (XRD). Prepared powder samples are loaded into the holder and scanned on a Rigaku Ultima IV diffractometer (Rigaku Corporation, Tokyo, Japan) (Cu-Kα radiation, λ = 1.5418 Å) across 5–90° 2θ, using a step size of 0.02° and a scan rate of 5°/min.

TGA is performed with the aid of a Netzsch STA 449 F5 synchronous thermal analyzer (Netzsch Gerätebau GmbH, Selb, Germany), which originates from Germany. For the test, a precisely measured 10–20 mg portion of the preconditioned powder is positioned within an alumina container. Throughout the procedure, the sample is subjected to a nitrogen environment while it is heated at a consistent rate of 10 °C per minute, spanning a temperature range from 30 °C to 1000 °C.

The mercury intrusion porosimetry (MIP) method is employed to determine the porosity characteristics of the samples. A 0.8 g pretreated powder is weighed, and the pore distribution is determined using an Auto Pore V 9620 mercury porosimeter (Micromeritics Instrument Corporation, Norcross, GA, USA) within a pressure range of 0.1–61,000 psi, with a contact angle set to 130°.

Microstructural and pore features are examined using a ZEISS Gemini SEM 300 (Carl Zeiss AG, Oberkochen, Germany). Prepared solid samples are mounted on conductive adhesive and coated with gold using a Quorum SC7620 sputter coater (Quorum Technologies Ltd., Laughton, East Sussex, UK) at 10 mA for 45 s. Morphology is imaged with an SE2 detector (Carl Zeiss AG, Oberkochen, Germany) at a 3 kV accelerating voltage.

3. Results and Analysis

To investigate particle size effects on shrinkage behavior and its interactions with activator parameters, the 29 specimens were categorized into three distinct subsets by WCP-R: 15.2 μm (n = 7), 24.4 μm (n = 15), and 33.6 μm (n = 7). With particle size held invariant within each subset, parameter interactions were probed through systematic variation in AM, AC, and W/S. Comparative analysis of shrinkage curves elucidated differential sensitivity to mix parameters across particle size regimes.

3.1. The Influence of Mix Factors on HWAASM's Drying Shrinkage

Figure 4 stratifies specimens by WCP-R to probe interactions with activator parameters. Per subset, shrinkage curves under varied AM/AC/W/S combinations delineate particle size-dependent sensitivity modulation. A comparison of Figure 4a,d indicates that as the WCP-R increases, the overall drying shrinkage tends to decrease. WCP-R = 15.2 μm leads

to greater drying shrinkage, mainly owing to their greater specific surface area, which facilitates the formation of C-A-S-H gel and elevates capillary pressure [45], while WCP-R = 33.6 μm results in relatively smaller shrinkage as coarse particles act as inert fillers, retaining crystalline phases that stabilize the matrix [37]. Meanwhile, the drying shrinkage values in Figure 4b,c are lower than those in Figure 4a but slightly higher compared to Figure 4d. This indicates that at a particle size of 24.4 μm, the drying shrinkage is relatively stable. In each figure, different HWAASM mixes with varying activator modulus ratios exhibit distinct trends. For example, samples with an AM of 1.6 generally show lower drying shrinkage, particularly R1M3A2W2 in Figure 4a and R2M3A1W2 in Figure 4c. This suggests that a higher AM contributes to reduced drying shrinkage, consistent with Aydin et al. [19], where elevated SiO_2/Na_2O ratio densifies gel structure and reduces >50 nm pores to restrict moisture migration [46]. On the other hand, samples with a lower AM (e.g., 1.2), such as R1M1A2W2, R1M2A1W2, and R2M1A1W2, display higher shrinkage, especially in the early stages.

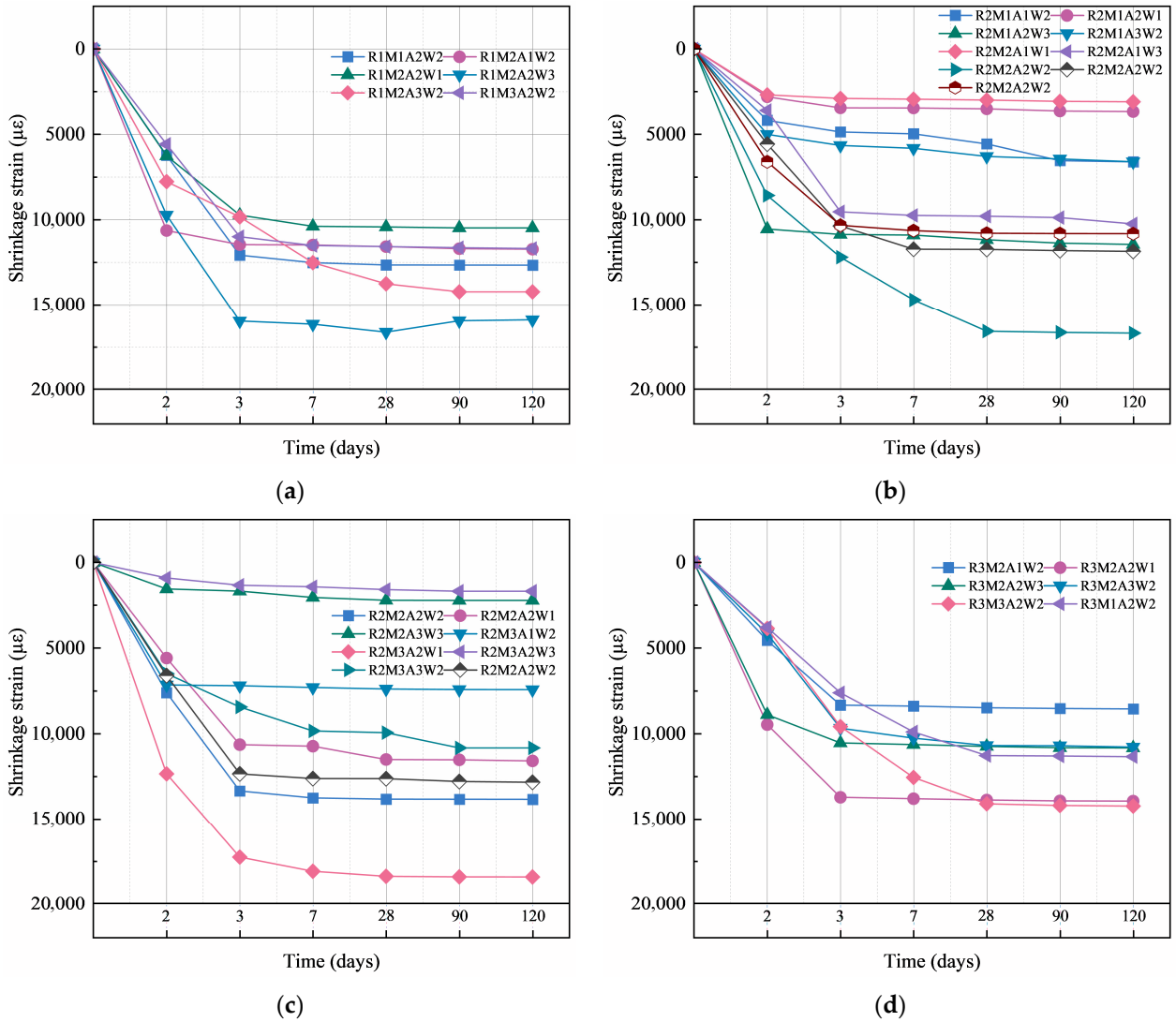

Figure 4. Drying shrinkage curves of HWAASM: (**a**) The effect of different activator parameters on shrinkage when WCP-R = 15.2 μm; (**b**,**c**) the effect of different activator parameters on shrinkage when WCP-R = 24.4 μm; and (**d**) the effect of different activator parameters on shrinkage when WCP-R = 33.6 μm.

The change in AC also has a significant impact on drying shrinkage. For instance, samples with an AC of 8% consistently show relatively higher drying shrinkage across the figures, particularly R1M2A3W2 in Figure 4a, R2M1A3W2 in Figure 4b, R2M2A2W1 in Figure 4c, and R3M2A2W1 in Figure 4d. This suggests that an increase in AC might lead to higher drying shrinkage. Conversely, samples with an AC of 6% or 7% exhibit smaller shrinkage, such as R1M1A2W2, R2M1A1W2, R2M2A2W2, and R3M2A1W2. Therefore, a moderate AC = 6–7% may help control the shrinkage behavior. The W/S also influences the drying shrinkage behavior. Most samples with a W/S of 0.48 show lower shrinkage than those with a W/S of 0.5, especially R1M2A2W3 in Figure 4a and R2M1A2W3 in Figure 4b, where higher shrinkage is observed with a 0.5 W/S. Mixes with a lower W/S = 0.46, including R1M2A2W1 in Figure 4a and R3M2A2W1 in Figure 4d, displayed reduced shrinkage. This is mechanistically attributed to reduced evaporable water content and optimized pore structure, minimizing capillary stresses—aligning with Liang, G et al. [32] reporting similar effects via ultrafine powder modification. The drying shrinkage curves in all figures show rapid shrinkage in the early stages, followed by a gradual stabilization. This indicates that moisture loss shrinkage is most significant in the early stage. As the AM increases, drying shrinkage tends to decrease, while higher AC and W/S lead to increased drying shrinkage. Although increasing particle size reduces shrinkage, its effect is less significant than that of the AC and AM. Through the analysis of the effects of different particle sizes, AM, AC, and W/S on the drying shrinkage behavior of HWAASM, it is evident that individual factors significantly impact the shrinkage. However, drying shrinkage behavior is often the result of multiple interacting factors. Therefore, the use of RSM to further analyze the interaction effects between these factors is essential.

3.2. Model Establishment and Analysis

A multivariate regression model was calibrated using WCP-R (A), AM (B), AC(C), and W/S (D) as predictors, optimized against 120-day drying shrinkage data from 29 HWAASM specimens. This process results in response Equation (2) and the fitted regression model for the 120-day drying shrinkage of HWAASM.

$$\begin{aligned} Y_{120d} &= 1.72 - 0.0948A + 0.1207B + 0.053C - 0.1075D + 0.033AB + 0.0492AC \\ &-0.3147AD + 0.0852BC - 0.6132BD - 0.4132CD + 0.1873A^2 - 0.1062B^2 - 0.3249C^2 - 0.2273D^2 \end{aligned} \quad (2)$$

Analysis of variance (ANOVA) is used in the model equation to assess the reliability and accuracy of the model. Taking the 120-day drying shrinkage regression model of HWAASM as an example, the ANOVA results are listed in Table 4.

For evaluating statistical significance, the *p*-value serves as a key metric in both hypothesis testing and assessing the goodness of fit. The model exhibits a *p*-value under 0.0001, reflecting high significance, and a lack-of-fit value above 0.05, affirming its reliability. A *p*-value below 0.05 suggests significant model terms, whereas a value above 0.10 indicates non-significant terms. Significant terms in this model include A, B, D, AD, BD, CD, A^2, B^2, C^2, and D^2. As shown in Table 5, the discrepancy between adjusted R^2 and predicted R^2 is under 0.2, indicating a well-fitted model.

Table 5. Result of model accuracy.

Model	Mean	C.V.%	R^2	Adjusted R^2	Predicted R^2	Adep Precision
120 day drying shrinkage	10,264.94	10.84	0.9629	0.9258	0.8345	19.0962

A signal to noise ratio (S/N) greater than 4 also suggests high model accuracy. Figure 5 demonstrates strong model validity through close alignment of predicted versus actual

values along the y = x reference. Figure 6 confirms residual normality via linear quantile–quantile distribution. Figure 7 exhibits homoscedasticity with randomized residual dispersion against predictions. This model robustly captures parametric control over HWAASM's 120-day drying shrinkage, quantitatively resolving multifactorial influences on contraction behavior. The applicability of this regression model is confined to the experimentally tested ranges, and extrapolated predictions beyond these boundaries may exhibit deviations.

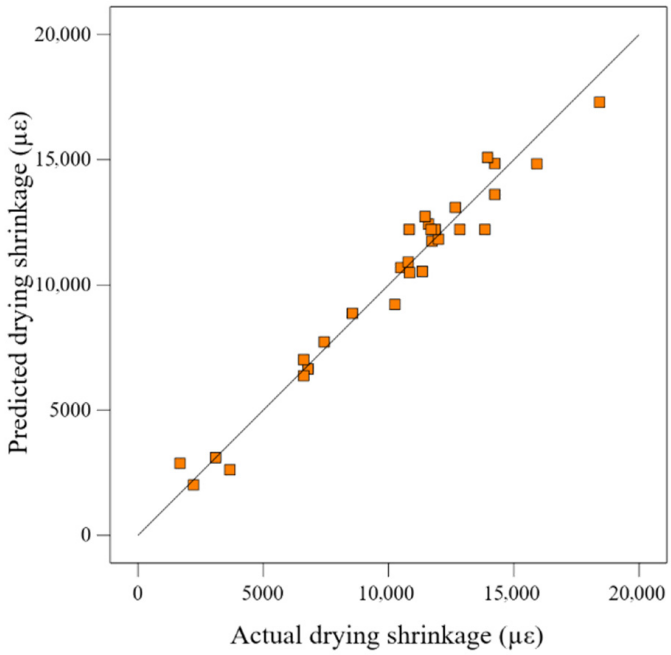

Figure 5. Actual value and predicted value.

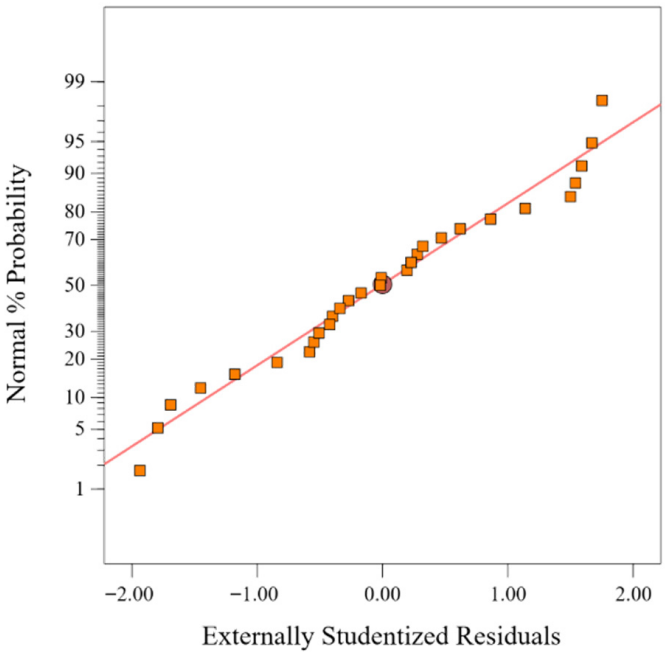

Figure 6. Normal probability distribution of model residuals.

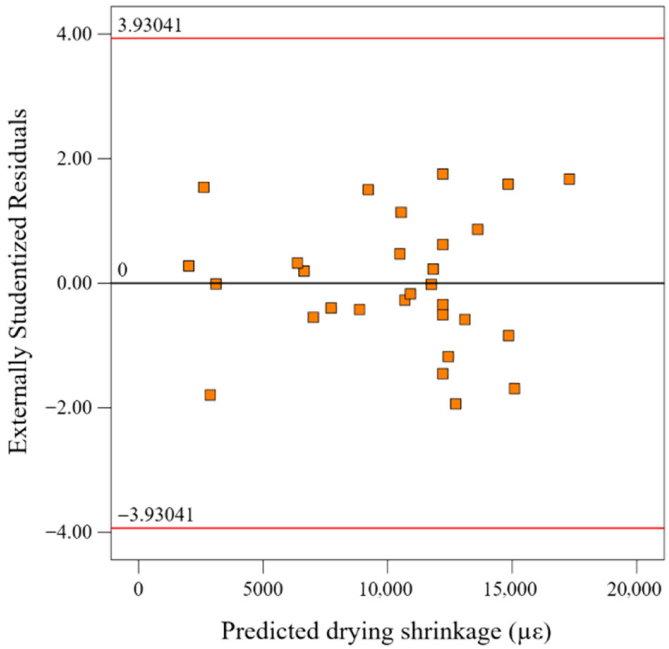

Figure 7. Analysis of the spread between predicted outcomes and actual residuals of the model.

3.3. RSM Analysis

Figure 8 illustrates the interactions among four factors: WCP-R, AM, AC, and W/S. As illustrated in Figure 8a, drying shrinkage declines steadily with increasing WCP-R from 15.2 μm to 33.6 μm in the AB-AC interaction plot. As the AM increases from 1.2 to 1.6, the change in drying shrinkage is relatively stable, with slightly higher shrinkage at an AM of 1.2, and the combination of 33.6 μm and an AM of 1.6 results in the lowest shrinkage. Figure 8b shows that as the WCP-R increases, drying shrinkage exhibits an overall decreasing trend. As the AC increases, shrinkage first increases and then decreases, forming a peak. The combination of a 15.2 μm WCP-R and a 6% AC leads to greater shrinkage, while the combination of a 33.6 μm WCP-R and an 8% AC results in lower shrinkage. Figure 8c shows that as the WCP-R increases, drying shrinkage gradually decreases. The combination of a 15.2 μm WCP-R and a 0.5 W/S produces the greatest shrinkage, while the combination of a 33.6 μm WCP-R and a 0.46 W/S results in the smallest shrinkage. Figure 8d shows that as the AM increases, drying shrinkage also increases, especially when the AC is 8%, where shrinkage reaches its maximum. When the AC is 6%, shrinkage is relatively smaller, but overall, shrinkage increases as the AM increases. Figure 8e shows a decreasing trend in shrinkage as the AM increases, particularly under W/S conditions, where shrinkage significantly decreases. Under higher AM and the condition of a 0.5 W/S, shrinkage remains high, and the impact of AM changes on shrinkage becomes more pronounced. Figure 8f shows that drying shrinkage gradually decreases as the AC increases, especially under lower W/S conditions, where the decrease is more evident. Under a higher W/S, shrinkage remains at a higher level, and the increase in AC from 6% to 8% has a more significant effect on shrinkage.

To further explain the drying shrinkage behavior of HWAASM, microstructural characterization is employed to reveal changes in the internal microstructure and chemical reaction processes of HWAASM. This study selects six samples (R3M3A2W2, R3M2A3W2, R3M2A2W3, R2M1A3W2, R2M1A2W3, R2M2A1W1) from the 29 response surface experiments for microstructural characterization, representing the minimum shrinkage values of two-factor interaction in the response surface analysis. The selected samples cover all key interaction effects, ensuring a systematic analysis of multi-variable influences. The

shrinkage values of the samples are distributed in the extreme value region of the response surface. By comparing their microstructural differences, the microstructural characteristics of the "optimal mix ratio" are clarified. The microstructural data of the samples directly validate the key conclusions of the response surface model. The statistical significance of all samples is verified through ANOVA ($p < 0.05$), and their microstructural features represent the core patterns of the response surface model.

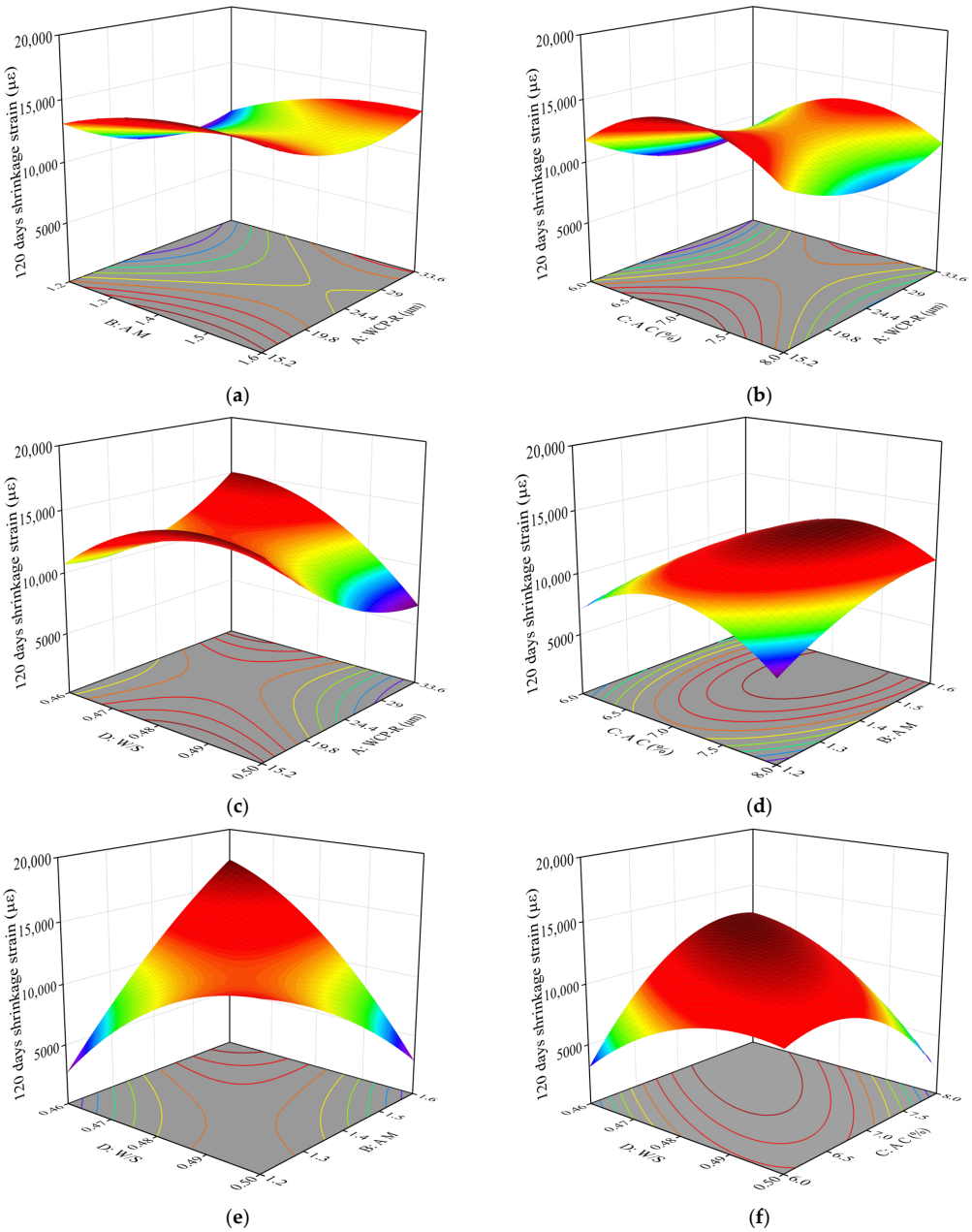

Figure 8. Response to the 120-day drying shrinkage of HWAASM. (**a**) Response of WCP-R and AM. (**b**) Response of WCP-R and AC. (**c**) Response of WCP-R and W/S. (**d**) Response of AM and AC. (**e**) Response of AM and W/S. (**f**) Response of AC and W/S.

3.4. Microstructure

3.4.1. Changes in the Reaction Products of HWAASM

Figure 9 displays the XRD patterns for the chosen samples of HWAASM. It can be observed that the crystalline phases of WCP, such as calcite and quartz, are clearly retained in all HWAASM samples. As shown in Figure 9, the quartz crystalline phase peaks are

relatively consistent across the different HWAASM samples, but variations in WCP-R appear to affect the intensity of other peaks. In the R3M3A2W2 sample, particles with a WCP-R = 33.6 μm are present, exhibiting higher diffraction peaks compared to samples with WCP particles of 24.4 μm. This indicates that the crystalline phase content in these larger particles is higher, and compared to smaller WCP particles, the crystalline structure of the larger WCP particles is not significantly disrupted. Changes in the AM also impact the crystalline phase behavior. For example, the differences between R3M3A2W2 (AM = 1.6) and R2M2A1W1 (AM = 1.4) reflect the influence of AM on crystalline phase changes. As WCP-R increases, the intensity of the crystalline diffraction peaks changes. Specimens featuring a WCP-R of 33.6 μm, such as R3M3A2W2, R3M2A3W2, and R3M2A2W3, typically show higher diffraction peaks than those with smaller WCP-R, like R2M2A1W1 and R2M1A3W2. The larger particle size reduces the amorphous phase content in HWAASM, enhancing the presence of crystalline phases. The AC also influences the strength of the diffraction peaks. For instance, R3M2A3W2 and R2M1A3W2 with 8% AC have stronger diffraction peaks, indicating that higher AC facilitates the formation of more crystalline phases. Variations in the W/S and AM also affect the amorphous phase content. Higher W/S, such as 0.5 in R2M1A2W3 and R3M2A2W3, promote the formation of gel phases, reducing the crystallinity of HWAASM and leading to an increase in the amorphous phase. Despite peak overlap around 26.6° 2θ, C-A-S-H is distinguished from crystalline quartz by its broad diffuse scattering in XRD patterns (15–35° 2θ), where the intensity of the amorphous hump relative to the baseline confirms the formation of the gel. This is closely related to the reaction characteristics of the AAS system, where the reaction rate and the type of products change due to adjustments in the W/S and AM. [26,47].

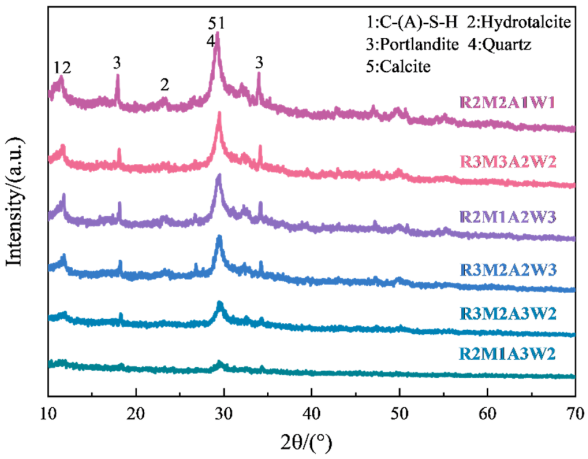

Figure 9. XRD patterns of HWAASM: C-(A)-S-H ($1.5CaO{\cdot}SiO_3{\cdot}xH_2O$, PDF # 33-0306), Hydrotalcite ($Mg_6Al_2(CO_3)(OH)_{16}{\cdot}4H_2O$, PDF # 41-1428), Portlandite ($Ca(OH)_2$, PDF # 87-0673), Quartz (SiO_2, PDF # 46-1045), Calcite ($CaCO_3$, PDF # 05-0586).

3.4.2. Thermogravimetric Analysis of HWAASM

The TGA results of different HWAASM samples are shown in Figure 10. The TG curves represent the mass loss of HWAASM samples at different temperatures. By comparing the TG curves of various samples, the mass loss in different temperature ranges is analyzed, reflecting the dehydration and decomposition of reaction products in HWAASM. The DTG curves provide the rate of mass loss as a function of temperature, indicating the decomposition of substances at different temperatures.

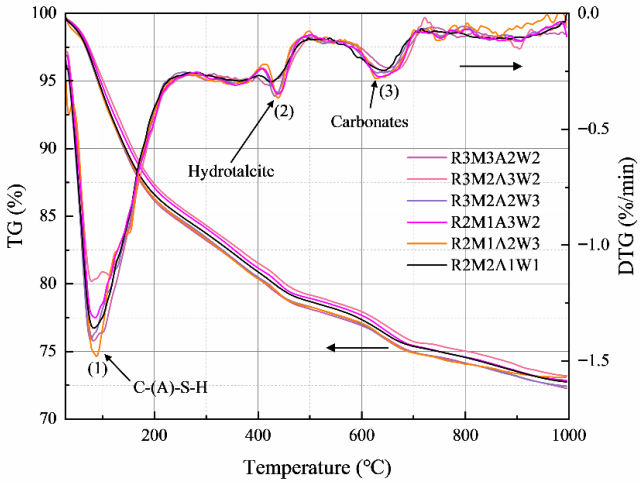

Figure 10. TG/DTG curves of HWAASM.

Dehydroxylation of C-(A)-S-H gels governs mass reductions between 30 and 200 °C [32,38,48]. When examining the TG curves, it is evident that the samples R3M3A2W2, R2M1A2W3, and R2M2A1W1 experience a greater degree of mass reduction. Elevated mass losses correlate with advanced reaction extents, promoting C-(A)-S-H gel proliferation. This is further corroborated by comparing the DTG curves, for R3M3A2W2 and R2M2A1W1 peaks located around 100 °C show larger intensity. In contrast, R3M2A3W2 and R3M2A2W3 show smaller peaks. Hydrotalcite thermolysis leads to to mass deficits within 200–400 °C [27,49,50]. The sample R3M2A2W3 shows the greatest mass reduction within this temperature range, which can be attributed to its elevated levels of hydrotalcite. This mineral is commonly found in alkali-activated systems and contributes to the long-term stability of HWAASM. The DTG curve for R3M2A2W3 shows a large peak around 400 °C, indicating a higher hydrotalcite content, suggesting that more minerals are generated in the AAS system. In contrast, R3M2A3W2 and R2M1A3W2 show smaller peaks, indicating lower hydrotalcite content. At temperatures between 600 °C and 800 °C, the mass loss is related to the decomposition of calcite [11,51]. The calcite content in R3M3A2W2 and R2M2A1W1 is significantly higher, indicating that most of the WCP particles in these samples do not participate in the alkali activation reaction, acting as a filler [37]. In contrast, R3M2A2W3, R2M1A3W2, and R3M2A3W2 show less mass loss in this range, indicating lower calcite content in these samples. Distinctive endothermic signatures near 650 °C in DTG profiles (R3M3A2W2/R2M2A1W1) confirm elevated residual calcite fractions. In contrast, R2M1A3W2 and R3M2A2W3 show smaller peaks, indicating relatively lower calcite content in these samples.

3.4.3. Analysis of Pore Structure in HWAASM

Figure 11 presents the cumulative pore volume and differential intrusion curves of samples with different mix design parameters. This study explores the effect of these parameters on drying shrinkage behavior, specifically in terms of pore size distribution, pore number, pore volume, and their connectivity. The pore size range is defined according to the classification standard [51], where micropores are defined as having diameters < 0.01 μm, mesopores range between 0.01 μm and 0.05 μm, and macropores have diameters > 0.05 μm. Table 6 lists the parameters that reflect the internal pore structure.

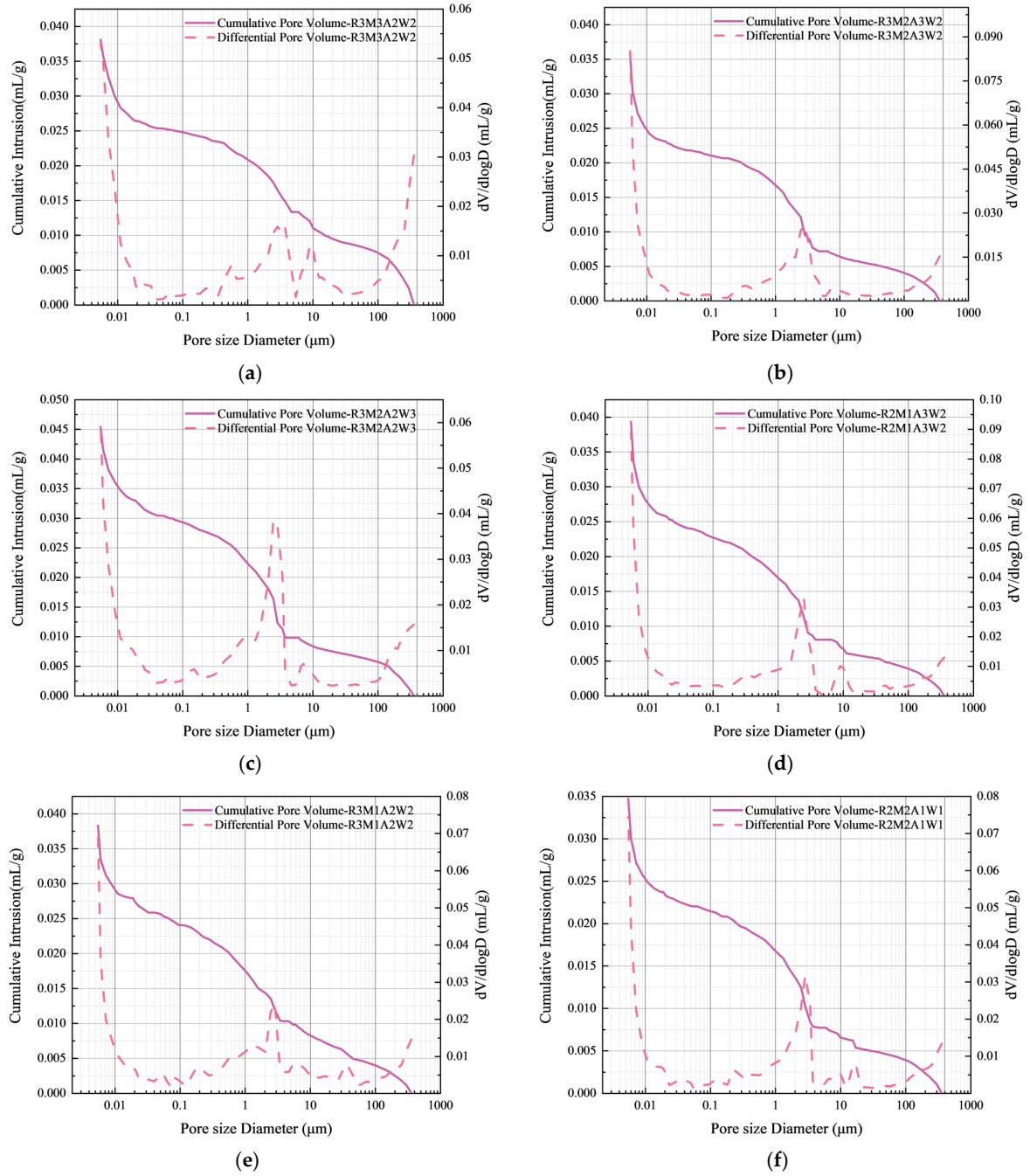

Figure 11. Cumulative pore volume and differential intrusion curves of HWAASM. (**a**) R3M3A2W2. (**b**) R3M2A3W2. (**c**) R3M2A2W3. (**d**) R2M1A3W2. (**e**) R3M1A2W2. (**f**) R2M2A1W1.

Table 6. Parameters of pore structure in HWAASM.

Serial Number	Total Intrusion Volume (mL/g)	Total Pore Area (m^2/g)	Median Pore Diameter (Area) (nm)	Apparent Density (g/mL)	Porosity (%)
R3M3A2W2	0.0381	6.269	6.92	2.1935	7.7149
R3M2A3W2	0.0401	9.466	6.55	2.1354	7.8895
R3M2A2W3	0.0482	8.157	7.06	2.1547	9.4161
R2M1A3W2	0.0435	9.892	6.62	2.1269	8.4668
R2M1A2W3	0.0497	11.873	6.76	2.1255	9.5470
R2M2A1W1	0.0383	8.173	6.59	2.1673	7.6698

First, the quantity of macropores and mesopores plays a key role across different samples. For the R3M3A2W2 and R3M2A2W3 samples, pores are mainly distributed within the macropore (>0.05 μm) and mesopore (0.01–0.05 μm) ranges. The MIP curve shows a pronounced intrusion peak between 0.01 μm and 0.1 μm, indicating that pores in this size interval dominate the total pore volume. The presence of these macropores and mesopores increases the migration and evaporation of moisture, exacerbating drying shrinkage [45,52]. Especially in R3M2A2W3, the number of macropores increases significantly, resulting in a larger cumulative pore volume, higher porosity, and thus a greater risk of shrinkage. In contrast, R3M2A3W2 exhibits smaller pores, mainly in the 0.01–0.05 μm mesopore range. Although the cumulative pore volume is smaller, the number of mesopores is still considerable, resulting in slower moisture movement [46], and consequently, milder shrinkage. Second, cumulative pore volume is closely related to shrinkage performance. R2M1A2W3 and R2M1A3W2 have larger cumulative pore volumes, indicating higher porosity, which is generally associated with a higher risk of shrinkage. In particular, the widespread distribution of mesopores in R2M1A2W3 accelerates moisture migration, leading to significant drying shrinkage. However, R2M2A1W1 has the smallest cumulative pore volume, indicating lower porosity, slower moisture evaporation, and thus, the least shrinkage. Lastly, pore connectivity also plays an important role in influencing the shrinkage of HWAASM. A higher number of mesopores and macropores, such as in R3M3A2W2 and R3M2A2W3, provide greater connectivity, facilitating rapid moisture migration and evaporation, resulting in significant shrinkage. In contrast, R2M1A3W2 and R2M2A1W1 have smaller pore sizes and lower porosity, resulting in poorer pore connectivity, reduced moisture migration, and less shrinkage. Overall, in the HWAASM samples, smaller particle sizes 24.4 μm help reduce total pore volume, particularly by limiting the formation of macropores, thus promoting material densification. An elevated activator modulus, AM = 1.6, decreases the volume of macropores while raising the share of mesopores and micropores, resulting in a more compact matrix. A higher AC of 8% improves reaction efficiency and reduces the formation of macropores, but if the W/S is not suitable, it can result in the formation of more pores. A lower W/S = 0.46 typically reduces pore volume, while a higher W/S = 0.5 often increases porosity, especially in the macropore range.

3.4.4. Analysis of Matrix Uniformity of HWAASM

Figure 12a–f display the SEM images of six HWAASM samples. We compare the morphology of pores, cracks, and reaction products to evaluate the influence of different mix design parameters on matrix homogeneity. Figure 12a,b compare samples R3M3A2W2 and R3M2A3W2, which share the same WCP size = 33.6 μm and W/S = 0.48 but differ in AM and content. R3M3A2W2, with a higher AM and moderate AC, exhibits fewer pores and cracks, and a uniform distribution of reaction products, indicating higher matrix density. In contrast, R3M2A3W2 has a lower AM and higher AC, resulting in increased cracks and larger pores. Although reaction products remain abundant, the faster reaction rate introduces more defects, leading to poorer matrix homogeneity. The comparison demonstrates that a higher AM helps reduce cracks and improve matrix density, while an excessive AC can increase the formation of cracks and pores. Second, R3M2A2W3, illustrated in Figure 12c, and R2M1A2W3, illustrated in Figure 12e, provide a contrast due to their different WCP-R = 33.6 μm and 24.4 μm, variations in W/S, and AM of 1.4 and 1.2, which significantly affect matrix homogeneity. R3M2A2W3 displays larger pores and more cracks, reflecting accelerated moisture migration and increased porosity at the higher W/S, which increases the risk of drying shrinkage [53]. In comparison, R2M1A2W3, with a smaller particle size of 24.4 μm, also has a high W/S (0.5), but the lower AM of 1.2 exacerbates the formation of cracks and pores, indicating that an imbalance between

the W/S and AM compromises matrix homogeneity. This comparison suggests that while the W/S is crucial in determining pore and crack formation [54], a lower AM combined with a higher W/S may make the matrix more vulnerable, increasing the risk of drying shrinkage. Lastly, R2M1A3W2, depicted in Figure 12d, and R2M2A1W1, depicted in Figure 12f, have the same WCP-R of 24.4 µm, but their W/S, AC, and AM differ, resulting in significant structural differences. R2M1A3W2, with a W/S of 0.48, higher AC = 8%, and lower AM = 1.2, shows more cracks and pores, along with uneven distribution of reaction products, leading to a less dense matrix. In contrast, R2M2A1W1, with the lowest W/S = 0.46, moderate AC = 6%, and an AM of 1.4, exhibits fewer cracks and smaller pores, with a more uniform distribution of reaction products, indicating better matrix density. This comparison clearly demonstrates that a lower W/S and moderate AC contribute to reduced porosity and improved matrix homogeneity.

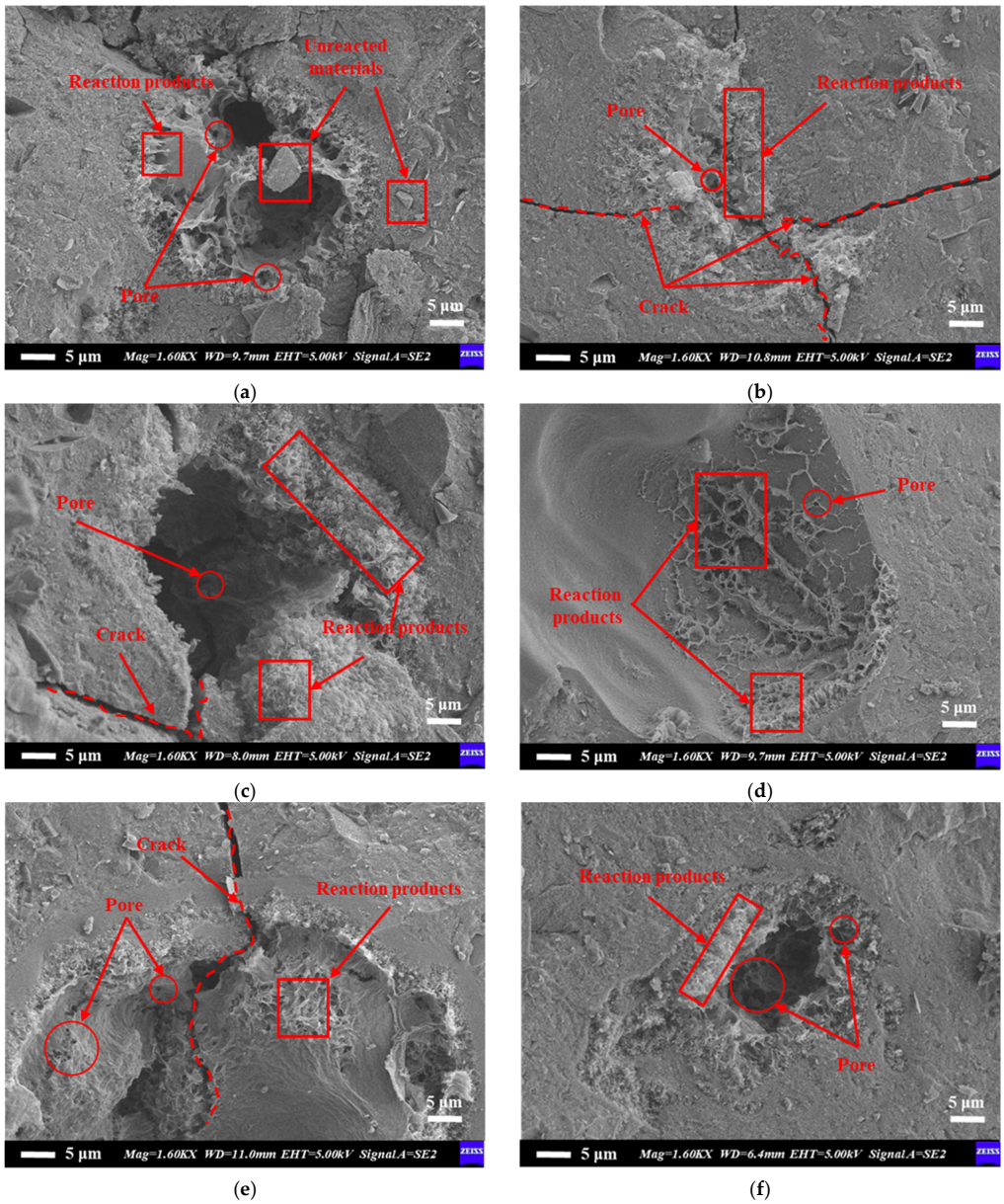

Figure 12. SEM Images of microstructure and matrix uniformity of HWAASM. (**a**) R3M3A2W2. (**b**) R3M2A3W2. (**c**) R3M2A2W3. (**d**) R2M1A3W2. (**e**) R3M1A2W2. (**f**) R2M2A1W1.

3.5. Discussion

This study adopts a high-dosage WCP-RSM co-optimization strategy and directly compares performance and mechanism with the literature data obtained at low WCP replacement levels. The optimized mix (60% WCP) exhibits a 120-day drying shrinkage of 1450.1 με, which is substantially lower than the 3000–6000 με typically reported for conventional AAS mortars [16,19,21] and well below the 3000 με threshold regarded as practically acceptable [19–21]. Moreover, despite the doubled WCP content, the corresponding concrete exhibits lower shrinkage than low-dosage (≤30%) systems. Notably, the minimum shrinkage value achieved in this study is even lower than the minimum reported by Zhang, D et al. [4] at 30% WCP. Furthermore, compared with a pure slag activated system, the mix containing 60% WCP exhibited 30% reduction in shrinkage. This reduction exceeds both that of 18.7–26.2% observed in 50% WCP mixes [55] and the 27.87% reduction reported by Liang, G et al. [32] using only 9% ultrafine WCP. In low-dosage systems, WCP acts mainly as a supplementary cementitious material, refining the gel through its reactivity. In the present 60% system, however, the coarser WCP fraction (33.6 μm) rich in crystalline phases shifts its primary role from reactive participant to physical filler and forming a rigid skeleton, thereby enhancing microstructural stability and mitigating drying shrinkage. The RSM model reveals a highly significant ($p < 0.0001$) negative interaction between the activator modulus and water to solid ratio (BD) on drying shrinkage. This indicates that the synergistic combination of a high activator modulus (AM) and low W/S ratio is crucial for developing a dense microstructure. As evidenced by MIP and SEM analyses, particularly when comparing specimens R2M2A1W1 and R2M1A2W3, this combination simultaneously promotes the formation of a low-calcium, highly polymerized C-A-S-H gel through the effect of high AM and reduces total porosity and capillary pore volume through low W/S. The joint effect significantly decreases the fraction of harmful large pores (>0.05 μm), thereby diminishing the internal capillary stress and mitigating the driving force for drying shrinkage. Regarding AC, the RSM offers deeper insight than single-factor analysis. Although the linear term of AC is non-significant ($p = 0.1212$), its quadratic term (C^2) is highly significant ($p < 0.0001$). This indicates a strong non-linear relationship, with an unmistakable optimum around 6.03%, rather than a simple "the lower, the better" trend. Near this optimum range (6–7%), AC effectively drives the reaction without inflicting noticeable structural damage. Deviating in either direction raises shrinkage: insufficient AC leads to an incomplete reaction and a weaker matrix, whereas excessive AC evident in SEM micrographs induces localized stress and defective pores due to overly localized reactions, ultimately increasing long-term shrinkage.

Correlating RSM with microstructure results, this study clarifies the drying shrinkage mechanism of high-WCP AASM: the difference between low- and high-shrinkage specimens is governed not by single factors but by the synergistic interaction of AM and W/S and AC and W/S (both $p < 0.0001$). R2M3A2W3 exploits the AM and W/S term dense gel forms, while moderate water prevents micro-defects, yielding 1682 με. The low shrinkage of R2M2A3W3 (2220 με) stems from the synergistic effect of high AC and an appropriate W/S: the high alkali promotes a more complete reaction, while the well-matched water content ensures a uniform microstructure. In contrast, the center point sample lacks this synergy and therefore exhibit average performance. Microstructural analysis further confirms that low-shrinkage mixes possess a denser matrix, lower total porosity, and significantly fewer harmful large pores (>0.05 μm), collectively contributing to their superior shrinkage resistance.

The RSM analyzes the interactions between multiple parameters through 29 experimental runs, reducing the experimental volume by about 70% compared to the traditional univariate trial-and-error method. The experimental scheme with 60% WCP substitution

for slag reduces the slag consumption of the mortar mix by approximately 240 kg (based on a density of 2.0 g/cm^3). Calculating for an annual production of 100,000 cubic meters of HWAASM, this can absorb 60,000 tons of construction waste powder, directly reducing the extraction of natural slag and alleviating resource shortage pressures. The carbon footprint of HWAASM mainly stems from activator production and the energy consumed in grinding WCP. According to lifecycle assessment (LCA) modeling [2], the optimized HWAASM has a carbon footprint of 180 kg CO_2-eq per ton. Traditional ordinary Portland cement (OPC) mortar emits about 800 kg CO_2-eq per ton, so the optimized mix cuts emissions by 77.5% [56]. This study demonstrates that WCP can serve as a functional binder, promoting the formation of the "demolition–crushing–reuse" closed-loop industrial chain.

4. Conclusions

Through response surface optimization and multi-scale characterization, this work elucidates the drying shrinkage mechanisms in HWAASM. The main conclusions are as follows:

1. RSM optimization identifies a parameter window that delivers ultra-low drying shrinkage for HWAASM: WCP-R = 33.6 μm, AM = 1.23, AC = 6.03%, and W/S = 0.49. Sample R2M3A2W3, whose settings fall within this window, records 1682.2 με, matching the model prediction and markedly below the values typical of conventional AAS.
2. Larger WCP particles (33.6 μm) mainly act as fillers due to their high crystalline phase content (calcite, quartz), which suppresses shrinkage. WCP particles that are smaller in scale (15.2 μm) encourage the creation of the amorphous phase via nucleation, although this can concurrently heighten the propensity for shrinkage.
3. A high AM (1.6) reduces the large pore ratio (<0.05 μm) and optimizes the pore distribution. A low W/S (0.46) reduces the total porosity to 7.67%, effectively limiting moisture migration and thereby suppressing shrinkage.
4. A combination of moderate AC (6–7%) and high AM (1.6) can reduce matrix cracking, while excessive AC (8%) accelerates the reaction and generates defective pores, leading to increased shrinkage.

Author Contributions: Conceptualization, Z.Z. and Y.Y.; methodology, Z.Z., H.G. and J.L.; software, Z.Z. and M.L.; data curation, Z.Z., J.L. and M.L.; writing—original draft preparation, Z.Z. and H.G.; writing—review and editing, Y.Z., J.L., M.L. and Y.Y.; formal analysis, Y.Z. and H.G.; supervision, Y.Z. and Y.Y. All authors have read and agreed to the published version of the manuscript.

Funding: This research was funded by the Sichuan Provincial Bureau of Geology and Mineral Exploration and Development Special Project (Grant No. SCDZ-DH202510) and the Research Foundation of Chongqing University of Science and Technology (Grant No. ckrc20241225).

Data Availability Statement: The raw data supporting the conclusions of this article will be made available by the authors on request.

Conflicts of Interest: The authors declare no conflicts of interest.

References

1. Amran, M.; Murali, G.; Khalid, N.H.A.; Fediuk, R.; Ozbakkaloglu, T.; Lee, Y.H.; Haruna, S.; Lee, Y.Y. Slag uses in making an ecofriendly and sustainable concrete: A review. *Constr. Build. Mater.* **2021**, *272*, 121942. [CrossRef]
2. Batuecas, E.; Ramón-Álvarez, I.; Sánchez-Delgado, S.; Torres-Carrasco, M. Carbon footprint and water use of alkali-activated and hybrid cement mortars. *J. Clean. Prod.* **2021**, *319*, 128653. [CrossRef]
3. Cai, R.; Ye, H. Clinkerless ultra-high strength concrete based on alkali-activated slag at high temperatures. *Cem. Concr. Res.* **2021**, *145*, 106465. [CrossRef]

4. Zhang, D.; Hao, W.; Yang, Q. Experimental Study on the Application of Recycled Concrete Waste Powder in Alkali-Activated Foamed Concrete. *Materials* **2023**, *16*, 5728. [CrossRef] [PubMed]
5. Zhang, P.; Wang, K.; Li, Q.; Wang, J.; Ling, Y. Fabrication and engineering properties of concretes based on geopolymers/alkali-activated binders—A review. *J. Clean. Prod.* **2020**, *258*, 120896. [CrossRef]
6. Ranjan, R.; Prusty, S.R.; Rout, B.; Panigrahi, R.; Jena, S. Assessing the effect of sodium nitrite as corrosion inhibitor against the corrosion of steel rebar in alkali-activated concrete. *J. Build. Eng.* **2024**, *92*, 109737. [CrossRef]
7. Shagñay, S.; Bautista, A.; Donaire, J.; Torres-Carrasco, M.; Bastidas, D.M.; Velasco, F. Chloride-induced corrosion of steel reinforcement in mortars manufactured with alternative environmentally-friendly binders. *Cem. Concr. Compos.* **2022**, *130*, 104557. [CrossRef]
8. Zhang, B.; Ma, Y.; Yang, Y.; Zheng, D.; Wang, Y.; Ji, T. Improving the high temperature resistance of alkali-activated slag paste using municipal solid waste incineration bottom ash. *J. Build. Eng.* **2023**, *72*, 106664. [CrossRef]
9. Wang, D.; Zhang, Z.; Shi, C.; Wang, Y.; Ren, Q.; Ning, C.; Liu, X.; Jiang, Z. Comparison study of ultra-high performance geopolymer concrete (UHPGC) and ultra-high performance concrete (UHPC): Mechanical properties, durability and carbon emissions. *Compos. B Eng.* **2025**, *307*, 112903. [CrossRef]
10. Yu, Y.; Al-Damad, I.M.A.; Foster, S.; Nezhad, A.A.; Hajimohammadi, A. Compressive strength prediction of fly ash/slag-based geopolymer concrete using EBA-optimised chemistry-informed interpretable deep learning model. *Dev. Built Environ.* **2025**, *23*, 100736. [CrossRef]
11. Seo, J.; Park, S.; Kim, G.M.; Park, S. Exploring natural and accelerated carbonation of alkali-activated slag. *Constr. Build. Mater.* **2024**, *432*, 136459. [CrossRef]
12. Liu, L.; Xu, Y.; Liu, H.; Xie, M.; He, Y.; Shi, C. Drying shrinkage and microstructure of alkali-activated slag with different mixing time at low temperatures (−5 to 5 °C). Constr. *Build. Mater.* **2022**, *360*, 129529. [CrossRef]
13. Bakharev, T.; Sanjayan, J.G.; Cheng, Y.B. Resistance of alkali-activated slag concrete to alkali–aggregate reaction. *Cem. Concr. Res.* **2001**, *31*, 331–334. [CrossRef]
14. Damrongwiriyanupap, N.; Wachum, A.; Khansamrit, K.; Detphan, S.; Hanjitsuwan, S.; Phoo-ngernkham, T.; Sukontasukkul, P.; Li, L.y.; Chindaprasirt, P. Improvement of recycled concrete aggregate using alkali-activated binder treatment. *Mater. Struct.* **2021**, *55*, 11. [CrossRef]
15. Tang, Q.; Ma, Z.; Wu, H.; Wang, W. The utilization of eco-friendly recycled powder from concrete and brick waste in new concrete: A critical review. *Cem. Concr. Compos.* **2020**, *114*, 103807. [CrossRef]
16. Gao, H.; Hamed, E.; Al-Damad, I.M.A.; Hajimohammadi, A.; Foster, S. Creep behaviour of alkali activated slag and fly ash concrete: Effects of hypothetical thickness, aggregates, and loading age. *Mater. Struct.* **2025**, *58*, 160. [CrossRef]
17. Fang, S.; Lam, E.S.S.; Li, B.; Wu, B. Effect of alkali contents, moduli and curing time on engineering properties of alkali activated slag. *Constr. Build. Mater.* **2020**, *249*, 118799. [CrossRef]
18. Zhang, P.; Kang, L.; Zheng, Y.; Zhang, T.; Zhang, B. Influence of SiO_2/Na_2O molar ratio on mechanical properties and durability of metakaolin-fly ash blend alkali-activated sustainable mortar incorporating manufactured sand. *J. Mater. Res. Technol.* **2022**, *18*, 3553–3563. [CrossRef]
19. Aydın, S.; Baradan, B. Effect of activator type and content on properties of alkali-activated slag mortars. *Compos. B Eng.* **2014**, *57*, 166–172. [CrossRef]
20. Liu, C.; Wu, H.; Li, Z.; Shi, H.; Ye, G. Effect of curing condition on mechanical properties and durability of alkali-activated slag mortar. *Constr. Build. Mater.* **2024**, *439*, 137376. [CrossRef]
21. Nanayakkara, O.; Gunasekara, C.; Sandanayake, M.; Law, D.W.; Nguyen, K.; Xia, J.; Setunge, S. Alkali activated slag concrete incorporating recycled aggregate concrete: Long term performance and sustainability aspect. *Constr. Build. Mater.* **2021**, *271*, 121512. [CrossRef]
22. *AS 3600:2018*; Concrete Structures. Standards Australia: Sydney, NSW, Australia, 2018.
23. Tan, W.; Xi, B. Toward Carbon Emission Reduction in Steel Production by Substituting Pulverized Coal and Coke with Biochar. *ACS EST Eng.* **2024**, *4*, 1253–1255. [CrossRef]
24. Tejas, S.; Pasla, D. Approach to design sustainable alkali-activated slag recycled aggregate concrete: Mechanical and microstructural characterization. *Case Stud. Constr. Mater.* **2024**, *21*, e03886. [CrossRef]
25. Sun, C.; Chen, L.; Xiao, J.; Singh, A.; Zeng, J. Compound utilization of construction and industrial waste as cementitious recycled powder in mortar. *Resour. Conserv. Recycl.* **2021**, *170*, 105561. [CrossRef]
26. Wang, X.; Yan, Y.; Tong, X.; Gong, Y. Investigation of Mineral Admixtures on Mechanical Properties of Alkali-Activated Waste concrete powders Cement. *Buildings* **2022**, *12*, 1234.
27. Horsakulthai, V. Effect of Waste concrete powder on strength, electrical resistivity, and water absorption of self-compacting mortars. *Case Stud. Constr. Mater.* **2021**, *15*, e00725.

28. Ren, P.; Li, B.; Yu, J.-G.; Ling, T.-C. Utilization of recycled concrete fines and powders to produce alkali-activated slag concrete blocks. *J. Clean. Prod.* **2020**, *267*, 122115. [CrossRef]
29. Zhu, H.; Shen, Z.; Li, Z.; Zhao, Z.; Shibo, L.; Yang, S.; Ruan, Z.; Ding, Y. Properties study of artificial aggregate with high-content Waste concrete powder. *J. Build. Eng.* **2023**, *78*, 107697.
30. Sasui, S.; Kim, G.; van Riessen, A.; Alam, S.F.; Nam, J.; Ishak, S.; Eu, H. Influence of elevated temperature on waste concrete powder and its application in alkali activated materials. *J. Clean. Prod.* **2024**, *434*, 140423. [CrossRef]
31. Liu, M.; Zhang, Y.; Wang, C.; Ma, Z. Reusing thermoactivated waste paste/concrete powder for sustainable alkali-activated materials: Effects of thermoactivated temperature. *Constr. Build. Mater.* **2024**, *437*, 136973. [CrossRef]
32. Liang, G.; Liu, T.; Li, H.; Wu, K. Shrinkage mitigation, strength enhancement and microstructure improvement of alkali-activated slag/fly ash binders by ultrafine waste concrete powder. *Compos. B Eng.* **2022**, *231*, 109570. [CrossRef]
33. Mäkelä, M. Experimental design and response surface methodology in energy applications: A tutorial review. *Energy Conv. Manag.* **2017**, *151*, 630–640. [CrossRef]
34. Yu, Y.; Rashidi, M.; Dorafshan, S.; Farsangi, E.N.; Yi, S.; Ding, Z. Ground penetrating radar-based automated defect identification of bridge decks: A hybrid approach. *J. Civ. Struct. Health* **2025**, *15*, 521–543. [CrossRef]
35. Zhao, G.; Pan, X.; Yan, H.; Tian, J.; Han, Y.; Guan, H.; Ruan, Y.; Liu, B.; Chen, F. Optimization and characterization of GGBFS-FA based alkali-activated CLSM containing Shield-discharged soil using Box-Behnken response surface design method. *Case Stud. Constr. Mater.* **2024**, *21*, e03800. [CrossRef]
36. Aswed, K.K.; Hassan, M.S.; Al-Quraishi, H. Optimisation and Prediction of Fresh Ultra-High-Performance Concrete Properties Enhanced with Nanosilica. *J. Adv. Concr. Technol.* **2022**, *20*, 103–116. [CrossRef]
37. Huo, W.; Zhu, Z.; Sun, H.; Gao, Q.; Zhang, J.; Wan, Y.; Zhang, C. Reaction kinetics, mechanical properties, and microstructure of nano-modified recycled concrete fine powder/slag based geopolymers. *J. Clean. Prod.* **2022**, *372*, 133715. [CrossRef]
38. Liu, M.; Wang, C.; Wu, H.; Yang, D.; Ma, Z. Reusing recycled powder as eco-friendly binder for sustainable GGBS-based geopolymer considering the effects of recycled powder type and replacement rate. *J. Clean. Prod.* **2022**, *364*, 132656. [CrossRef]
39. Liu, M.; Wu, H.; Yao, P.; Wang, C.; Ma, Z. Microstructure and macro properties of sustainable alkali-activated fly ash mortar with various construction waste fines as binder replacement up to 100%. *Cem. Concr. Compos.* **2022**, *134*, 104733. [CrossRef]
40. Liu, M.; Wu, H.; Yao, P.; Wang, C.; Ma, Z. Effect of ground concrete waste as green binder on the micro-macro properties of eco-friendly metakaolin-based geopolymer mortar. *J. Build. Eng.* **2023**, *68*, 106191. [CrossRef]
41. Wu, D.; Wang, J.; Miao, T.; Chen, K.; Zhang, Z. Performance Optimization of FA-GGBS Geopolymer Based on Response Surface Methodology. *Polymers* **2023**, *15*, 1881. [CrossRef]
42. Mousavi, S.; Gheibi, M.; Wacławek, S.; Smith, N.R.; Hajiaghaei-Keshteli, M.; Behzadian, K. Low-energy residential building optimisation for energy and comfort enhancement in semi-arid climate conditions. *Energy Conv. Manag.* **2023**, *291*, 117264. [CrossRef]
43. *JGJ/T 98-2011*; Specification for Mix Proportion Design of Masonry Mortar. Ministry of Housing and Urban–Rural Development of the People's Republic of China, China Architecture & Building Press: Beijing, China, 2011.
44. *JGJ/T 70-2009*; Standard for Test Methods of Basic Properties of Construction Mortar. Ministry of Housing and Urban–Rural Development of the People's Republic of China, China Architecture & Building Press: Beijing, China, 2009.
45. Ye, H.; Radlińska, A. Shrinkage mechanisms of alkali-activated slag. *Cem. Concr. Res.* **2016**, *88*, 126–135. [CrossRef]
46. Ye, H.; Cartwright, C.; Rajabipour, F.; Radlińska, A. Understanding the drying shrinkage performance of alkali-activated slag mortars. *Cem. Concr. Compos.* **2017**, *76*, 13–24. [CrossRef]
47. Rashad, A.M.; Said, N.; Abdel-Gawwad, H.A. An initial study about the effect of activated carbon nano-sheets from residual biomass of olive trees pellets on the properties of alkali-activated slag pastes. *J. Build. Eng.* **2021**, *44*, 102661.
48. Baggio, T.F.; Possan, E.; de Oliveira Andrade, J.J. Physical-chemical characterization of construction and demolition waste powder with thermomechanical activation for use as supplementary cementitious material. *Constr. Build. Mater.* **2024**, *437*, 136907. [CrossRef]
49. Ye, H.; Huang, L.; Chen, Z. Influence of activator composition on the chloride binding capacity of alkali-activated slag. *Cem. Concr. Compos.* **2019**, *104*, 103368. [CrossRef]
50. Liu, J.; Tian, Y.; Ge, X.; Liu, B.; Liu, K.; Song, G. Experimental Study on MgO-Na_2CO_3 Combined Excitation Recycled Fine-Powder-Slag Cementitious System and Modification. *Buildings* **2024**, *14*, 592. [CrossRef]
51. Zhang, X.Y.; Fan, M.X.; Zhou, Y.X.; Ji, D.D.; Li, J.H.; Yu, R. Development of a sustainable alkali activated ultra-high performance concrete (A-UHPC) incorporating recycled concrete fines. *J. Build. Eng.* **2023**, *67*, 105986. [CrossRef]
52. Gao, H.; Shikhov, I.; Hamed, E.; Hajimohammadi, A.; Al-Damad, I.; Arns, C.; Foster, S.J. New insights on the basic creep mechanism of one-part alkali activated slag and fly ash paste. *Cem. Concr. Res.* **2024**, *186*, 107691. [CrossRef]
53. Huo, W.; Zhu, Z.; Sun, H.; Yang, L.; Zhang, C. Estimating the relationships between initial constituent molar ratios and physical–mechanical properties of RCFP-GBFS based geopolymers. *Constr. Build. Mater.* **2023**, *406*, 133409. [CrossRef]

54. Su, C.; Zhang, J.; Ding, Y. Research on reactivity evaluation and micro-mechanism of various solid waste powders for alkali-activated cementitious materials. *Constr. Build. Mater.* **2023**, *411*, 134374. [CrossRef]
55. Turner, L.K.; Collins, F.G. Carbon dioxide equivalent (CO_2-e) emissions: A comparison between geopolymer and OPC cement concrete. *Constr. Build. Mater.* **2013**, *43*, 125–130. [CrossRef]
56. Provis, J.L. Alkali-activated materials. *Cem. Concr. Res.* **2018**, *114*, 40–48. [CrossRef]